Proceeding of the IEEE
International Conference on Robotics and Biomimetics
Dali, China, December 2019

SMA-actuated Morphing Wing with Varying Spanwise Curvature and Swept Angle*

Zhiqiang Wang ,Xiaojun Yang and Bing Li
School of Mechanical Engineering and Automation
Harbin Institute of Technology (Shenzhen)
Shenzhen, 518055, China
yangxiaojun@hit.edu.cn

***Abstract* –In this paper, a new morphing wing mechanism with two degrees of freedom is presented, which can realize the varying spanwise curvature and swept angle of the wing. The wing consists of segmented beams, flexible hinges, and a SMA actuator. A theoretical model of hinge's compliance matrix is established based on linear elastic material and small displacement. A finite element analysis (FEA) is used to analyze the flexible hinge in order to produce the compliance matrix. The results validates the theoretical model. A heating method is developed to improve the output response of the SMA-actuator. The presented mechanism is fabricated and the experimental results demonstrates the potential of this mechanism.**

Index Terms – Morphing wing; Flexible hinges; SMA actuator; Compliant mechanism

I. INTRODUCTION

With the increasing requirements of aircraft performance, such as military reconnaissance strikes, long-distance transportation and disaster relief, advanced aircraft have developed toward intelligent, high-efficiency and multi-task. In this case, the traditional rigid wing has been unable to meet the application requirements, and the morphing wing that can adapt to various flight tasks, different environmental conditions and achieve optimal flight performance has received increasing attention and research. Morphing wing refers to an adaptive deformable wing that can achieve multiple degrees of freedom, large scale, rapid deformation and real-time sensing of various loads and flight attitudes to adapt to different environments and different flight requirements. At present, the existing research has proved that the deformable wing can achieve continuous deformation, and the surface of the wing is smooth and flat, which can effectively improve the lift-to-drag ratio, and is particularly prominent in achieving lightweight, high flexibility and reducing flutter. There is great development space in both civil and military applications.

In 2004, NEAL used an electromechanical torsion mechanism to achieve sweep angle control, and the experimental prototype's range of sweep angle could reach 40° [1]. In 2012, Jinsong Leng and Qian Chen designed a large-scale variable swept wing based on scissor deformation mechanism, and verified the aerodynamic performance of the variable swept wing model through wind tunnel experiments [2]. Lawren L. Gamble evaluated the impact of morphing coupled sweep and camber at three different velocities. The numerical results suggest that there is a clear advantage in morphing both the sweep and the camber at varying velocities [3]. NASA's research shows that a wing with a curved span, an elliptical sweep, and a split elliptical span has better aerodynamics than a planar wing. In view of this, in terms of the varying spanwise curvature, WIGGINS studied the method of changing the warp direction curvature by using a single-degree-of-freedom scissor mechanism, and inputting the actuation load at one end of the scissor mechanism in 2004 [4]. The input load is put at one end of the scissor mechanism, and the overall deformation of the mechanism can be realized by the load transfer between the scissor units. In 2006, MANZO designed a wing structure with variable spanwise bending using a segmented mechanism, and respectively used shape memory alloy and DC motor drive mechanism deformation [5]. In this paper, a flexible deformation wing prototype is designed and manufactured, and the main structure of the prototype is modeled and analyzed. Finally, the performance of the morphing wing is verified by experiments.

II. WING PROTOTYPE

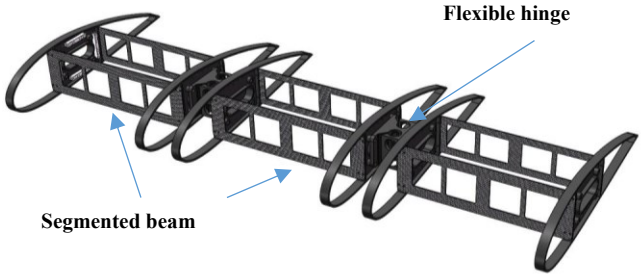

Fig. 1 CAD model of the morphing wing

A. Wing deformation scheme

This paper proposes a flexible hinge deformation structure, which uses a flexible joint connection between the chord-to-ribs of the wing, and the deflection of the flexible joint drives the entire wing to change the spanwise curvature angle and sweep angle of the wing; In addition, in consideration of the light weight requirement, the driving method selects the shape memory alloy wire actuator. The wing structure of the wing of the model adopts a segmented beam structure, which consist of front beam and back beam (Fig. 1). Under this spar structure, the wing ribs of the wing can maintain structural integrity and have better aerodynamic performance during the chordwise

* This work is partially supported by Shenzhen International Cooperation Programme (Grant No.GJHZ20170313113529978).

978-1-7281-6321-5/19//$31.00 ©2019 IEEE

bending process. At the same time, the segmented spar can meet the deformation requirements in the spanwise and sweep directions.

B. Main structure design

The main component of the wing that achieves varying spanwise curvature and sweep angle of the wing is a flexible hinge that differs from conventional hinges (Fig. 2a). It relies primarily on its own deformation to effect deformation of the wing. It can achieve flexible bending deformation in two directions.

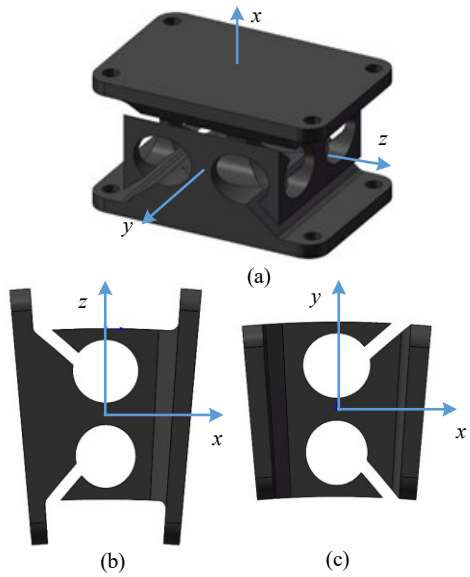

Fig.2 Flexible hinge: (a) Flexible hinge structure, (b) sweep angle deformation, (c) spanwise curvature deformation.

The wing airfoil used in this project is the NACA4421 low-speed wing. The relative curvature of the airfoil is 4%. The maximum camber is located at 40% of the leading edge of the chord with a relative thickness of 21%.

Depending on the size of the wing prototype shown in TABLE I, the model has a chord length of 280 mm and a model length of 680 mm.

TABLE I PROTOTYPE MODEL MAIN PARAMETERS

Parameters	Value	Unit
Body length	1320	mm
Wing length	1720	mm
Wing area	46.5	dm^2
Total Weight	2950	g
Airfoil load	64	g/dm^2

C. Shape memory alloy actuator

In recent years, a lot of research has been done on the actuators of wing. Table 2 compares the performance indexes of shape memory alloy and several common actuators. This table is adapted from [6]. It can be seen that the shape memory alloy has larger stress strain and lighter weight, although it's corresponding speed is slow.

TABLE II PERFORMANCE COMPARISON AMONG DIFFERENT ACTUATORS

Actuator Type	Max Strain	Max Actuation Stress (MPa)	Specific Work (J/kg)	Max Frequency (Hz)
SMA	0.07	700	4500	7
Piezoelectric	0.02	9	1	10^7
Magnetostrictive	0.002	200	20	10^7
Hydraulic Cylinder	1	70	35000	100
Solenoid	0.4	0.1	5	80

Shape memory alloys are widely used in flexible wings due to their single-stroke shape memory effect. When the shape memory alloy wire is shrunk, the biasing mechanism stretches the recovered shape memory alloy wire again for the next use. At present, in the flexible wing, depending on the arrangement, the application of the shape memory alloy actuator mainly includes a biasing actuator and a differential actuator. In addition, the manner of heating the shape memory alloy wire is also different. At present, there are mainly internal heating, external heating, and internal and external heating. Since this work needs to control the change of the wing angle actively, the differential actuator shown in Fig. 3 (a) is selected. Its implementation principle is shown in Fig. 4.

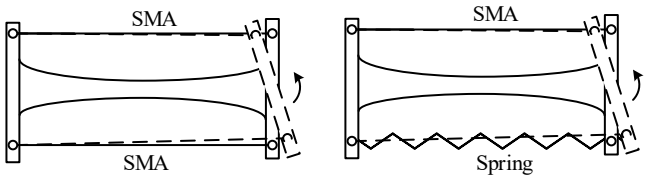

Fig. 3 Shape memory alloy wire actuator schematic
(a) Differential actuator, (b) Bias actuator

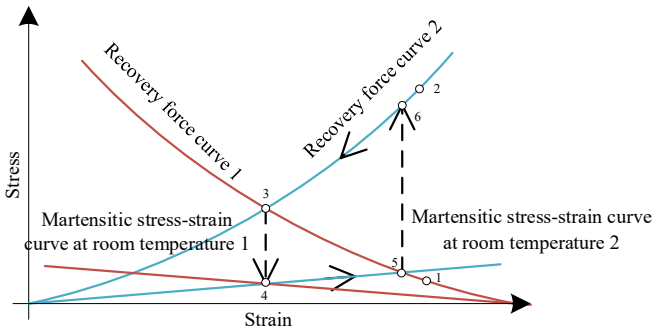

Fig. 4 Differential SMA actuator schematic

By controlling the magnitude of the current in the shape memory alloy wire connected to the wing rib, the deformation of the shape memory alloy wire can be controlled; by the difference between the upper and lower and the left and right deformations, the wing deflection and the grazing angle are respectively realized. The complete SMA actuator model is shown in Fig. 5.

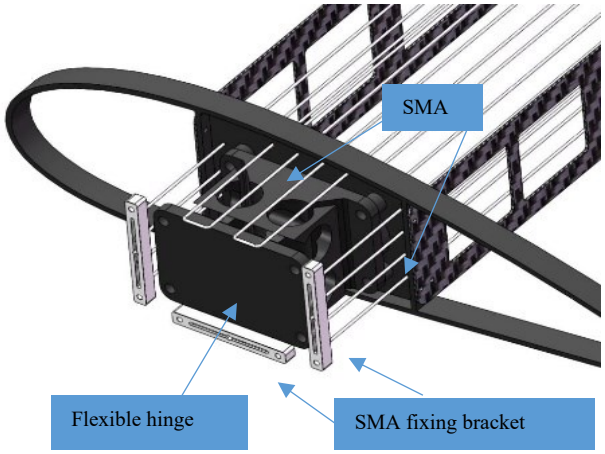

Fig. 5 SMA actuator

In addition, the response time of SMA under three different heating modes of internal heating, external heating and simultaneous internal and external heating was tested by experiments. Use a shape memory alloy wire with a length of 100mm.The thermocouple probes are arranged in an average of four positions. Sixteen sets of data were measured from the electrification. The tests were carried out under the condition of internal heating, external heating and simultaneous internal and external heating respectively.

The experimental results are shown in the Fig. 6. Among them, the internal heating is to heat the SMA, and the external heating is 0.15 mm in diameter. The varnished wire is tightly wrapped around the SMA wire, and the varnished wire is heated by electric heating. The internal and external heating is simultaneously heated to simultaneously heat the SMA and the varnished wire. It can be seen from the experimental results that the internal and external simultaneous heating of the SMA has a faster response speed and is more in line with the characteristics of the wing deformation requiring rapid response. Compared with the three methods, the first heating method can reach 44.3 degrees at 16 seconds, the second can reach 98 degrees, and the improved heating method can reach 117 degrees.

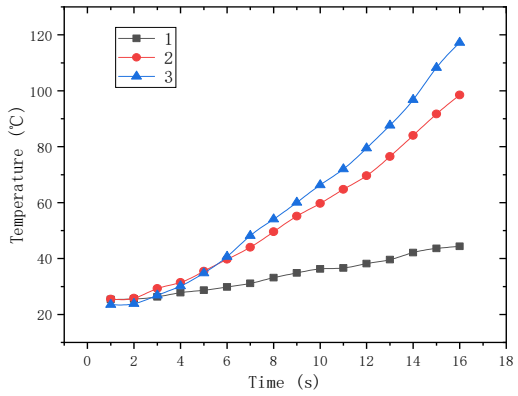

Fig. 6 Response of SMA actuators under different heating methods. 1-internal heating with 4.5A current, 2- external heating with 1.5A current, 3-Both of above.

III. PROTOTYPE MODELING

A. *Flexible structural mechanics modeling*

The flexible hinge is different from the conventional hinge, and mainly relies on its own deformation to realize the deformation of the wing. In this paper, the linear analytical model of the flexible mechanism is established by applying the research results of the flexible structure.

There is no direct analytical method for the compliant matrix of the structure, but by observing the structure, the structure can be decomposed into two combined flexible structures-two sets of unidirectional flexible hinges (called I-type) and two-axis flexible hinges (called Type II) inside the structure, as shown in Fig. 7.

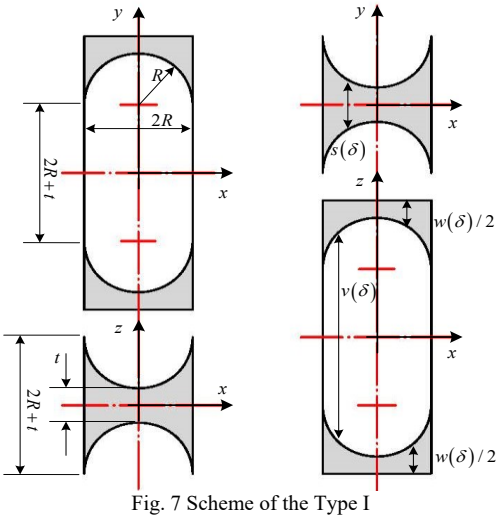

Fig. 7 Scheme of the Type I

There are two sets of uniaxial flexible hinges, which are rotated around the x-axis and the y-axis respectively, and are represented by I-y-axis and I-z-axis, respectively. The inner biaxial flexible hinge is represented by type II; respectively, two sets of flexibility are obtained. The flexibility matrix of the hinge can be obtained by combining the flexibility matrices of the hinges in parallel.

To understand the geometry of two unidirectional flexible hinges, the view of each structure (y-x plane on the left and z-x plane on the right), and both types have complete circular notches.

Regardless of the geometry of the flexible structure, the flexible hinge can be characterized by the elastic properties of one end (usually assumed to be the free end), while the other end is usually assumed to be a fixed end, as shown in Fig. 8.

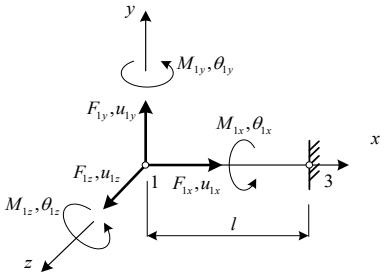

Fig. 8 Frame setting for loads and displacements

From this perspective, the free end 1 of the general form of the flexible hinge will have six degrees of freedom (DOF), three translations and three rotations produced by bending, axial

loading, respectively. Under the assumption of small displacement, the deformation vector at one point and the load vector at the same point have the relationship of Eq. (1).

$$\{\boldsymbol{u}\}=[\boldsymbol{C}]\{\boldsymbol{f}\} \tag{1}$$

Where $\boldsymbol{f}$ is the load vector

$$\boldsymbol{f}=\begin{bmatrix}F_x & F_y & F_z & M_x & M_y & M_z\end{bmatrix} \tag{2}$$

$\boldsymbol{u}$ is the displacement vector

$$\boldsymbol{u}=\begin{bmatrix}u_x & u_y & u_z & \theta_x & \theta_y & \theta_z\end{bmatrix} \tag{3}$$

And C is a 6×6 flexibility matrix. For the two-axis flexible hinge shown above, the symmetric compliance matrix is defined as follows

$$C=\begin{bmatrix} C_{u_x-F_x} & 0 & 0 & 0 & 0 & 0 \\ 0 & C_{u_y-F_y} & 0 & 0 & 0 & C_{u_y-M_z} \\ 0 & 0 & C_{u_z-F_z} & 0 & C_{u_z-M_y} & 0 \\ 0 & 0 & 0 & C_{\theta_x-M_x} & 0 & 0 \\ 0 & 0 & C_{u_z-M_y} & 0 & C_{\theta_y-M_y} & 0 \\ 0 & C_{u_y-M_z} & 0 & 0 & 0 & C_{\theta_z-M_z} \end{bmatrix} \tag{4}$$

According to the relevant theory of elastic mechanics, the displacement and rotation of a biaxial flexible hinge can be calculated according to Castiano's theorem (Carl's theorem), that is, the displacement in a certain force direction is equal to the total strain energy of the structure [7].

$$\begin{cases}\boldsymbol{u}_i=\dfrac{\partial \boldsymbol{U}}{\partial \boldsymbol{F}_i}, & i=x,y,z \\ \boldsymbol{u}_i=\dfrac{\partial \boldsymbol{U}}{\partial \boldsymbol{F}_i}\end{cases} \tag{5}$$

The flexible hinge can be considered a cantilever beam during operation. Thus, the total strain energy $\boldsymbol{U}$ of the structure includes tensile strain energy $\boldsymbol{U}_a$, along the z-axis, bending strain energies $\boldsymbol{U}_{by}$ and $\boldsymbol{U}_{bz}$, around the x-axis and the y-axis, and winding z. The torsional strain energy of the shaft is $\boldsymbol{U}_t$.

$$\boldsymbol{U}=\boldsymbol{U}_a+\boldsymbol{U}_{by}+\boldsymbol{U}_{bz}+\boldsymbol{U}_t \tag{6}$$

The expression of each strain energy is as shown in Eq. (7).

$$\begin{cases}\boldsymbol{U}_a=\displaystyle\int_0^l\frac{F_{1x}^2}{2EA(x)}dx \\ \boldsymbol{U}_{by}=\displaystyle\int_0^l\frac{\left(F_{1z}x+M_{1y}\right)^2}{2EI_y(x)}dx \\ \boldsymbol{U}_{bz}=\displaystyle\int_0^l\frac{\left(M_{1z}-F_{1y}x\right)^2}{2EI_z(x)}dx \\ \boldsymbol{U}_t=\displaystyle\int_0^l\frac{M_{1x}^2}{2GI_t(x)}dx\end{cases} \tag{7}$$

In the I-type structure, in order to facilitate the calculation, the coordinate origin is moved from the geometric center to the lower surface of the circular hole, and a new coordinate system is established, and the change of the independent variable is $\delta=x+R$.

According to the definition in the figure, the parameters used to describe the shape of the hinge are s(δ), ν(δ) and w(δ). According to the different shapes of the design, these parameters are also different. The initial design in the figure is a straight circle, and the figure can be obtained according to the calculation. The dimensional parameters of the straight circular hinge in Fig. 8 are as follows:

$$\begin{cases}s(\delta)=2R+t-2\sqrt{2R\delta-\delta^2} \\ v(\delta)=2R+t+2\sqrt{2R\delta-\delta^2} \\ w(\delta)=h-v\end{cases} \tag{8}$$

For the I-section in the figure, the area of the section is:

$$A(\delta)=w(\delta)\cdot s(\delta) \tag{9}$$

At the same time, the moment of inertia of the I-section can be determined as:

$$I_y=\frac{w(\delta)s(\delta)^3}{12},I_z=\frac{s(\delta)\left(h(\delta)^3-v(\delta)^3\right)}{12} \tag{10}$$

Substituting Eq. (6)-(10), into Eq. (5) yields

$$\begin{cases}u_{1x}=\dfrac{\partial U}{\partial F_{1x}}=\displaystyle\int_0^{2R}\frac{F_{1x}}{Ew(\delta)s(\delta)}d\delta \\ u_{1y}=\dfrac{\partial U}{\partial F_{1y}}=\displaystyle\int_0^{2R}\frac{12\delta^2F_{1y}}{Es(\delta)\left(h(\delta)^3-v(\delta)^3\right)}d\delta \\ -\displaystyle\int_0^{2R}\frac{12\delta M_{1z}}{Es(\delta)\left(h(\delta)^3-v(\delta)^3\right)}d\delta \\ u_{1z}=\dfrac{\partial U}{\partial F_{1z}}=\displaystyle\int_0^{2R}\frac{12\delta^2F_{1z}}{Ew(\delta)s(\delta)^3}d\delta+\int_0^{2R}\frac{12\delta M_{1y}}{Ew(\delta)s(\delta)^3}d\delta \\ \theta_{1x}=\dfrac{\partial U}{\partial M_{1x}}=\displaystyle\int_0^{2R}\frac{12\delta^2M_{1x}}{Ew(\delta)s(\delta)^3R_t^2}d\delta \\ \theta_{1y}=\dfrac{\partial U}{\partial M_{1y}}=\displaystyle\int_0^{2R}\frac{12\delta F_{1z}}{Ew(\delta)s(\delta)^3}d\delta+\int_0^{2R}\frac{12M_{1y}}{Ew(\delta)s(\delta)^3}d\delta \\ \theta_{1z}=\dfrac{\partial U}{\partial M_{1z}}=-\displaystyle\int_0^{2R}\frac{12\delta F_{1y}}{Es(\delta)\left(h(\delta)^3-v(\delta)^3\right)}d\delta \\ +\displaystyle\int_0^{2R}\frac{12M_{1z}}{Es(\delta)\left(h(\delta)^3-v(\delta)^3\right)}d\delta\end{cases} \tag{11}$$

In the above formula, let

$$\begin{aligned} I_1&=\int_0^{2R}\frac{1}{ws}d\delta & I_5&=\int_0^{2R}\frac{12\delta}{ws^3}d\delta \\ I_2&=\int_0^{2R}\frac{12\delta^2}{s\left(h^3-v^3\right)}d\delta & I_6&=\int_0^{2R}\frac{12\delta^2}{ws^3R_t^2}d\delta \\ I_3&=\int_0^{2R}\frac{12\delta}{s\left(h^3-v^3\right)}d\delta & I_7&=\int_0^{2R}\frac{12}{ws^3}d\delta \\ I_4&=\int_0^{2R}\frac{12\delta^2}{ws^3}d\delta & I_8&=\int_0^{2R}\frac{12}{s\left(h^3-v^3\right)}d\delta \end{aligned} \tag{12}$$

In the proposed calculation method, it is assumed that the torque is decomposable in two opposing forces that are perpendicular to the hinge plane and act on the point where the top radius of the hinge is R_t. These forces create additional bending moments on each side of the hinge. The resulting displacement relative to the right and left sides is converted to θ_z. As a result of the previous hypothesis, the integral I_8 is

obtained as a function of the bending terms I_2 and R_t. The radius R_t is assumed to be the distance between the z-axis and the centroid of one side of the hinge. After geometric calculations, it can be calculated and recalculated for different hole shapes [8] [9].

$$R_t = R + \frac{t}{2} + \frac{\left(\frac{h}{2} - R - \frac{t}{2}\right)^2 - \frac{2}{3}R^2}{h - t - \left(2 + \frac{\pi}{2}\right)R} \tag{13}$$

The simplified formula above can be written in the form of matrix multiplication. The two compliant matrices $\boldsymbol{C_{Az}}$ and $\boldsymbol{C_{Ay}}$ of the type I structure can be obtained according to the Eq. (4), and the overall flexibility matrix $\boldsymbol{C_A}$ of the type I in the flexible hinge is shown in Eq. (14).

$$\boldsymbol{C}_A = \boldsymbol{C}_{Az} + \boldsymbol{C}_{Ay} \tag{14}$$

$$C_{Ay} = \frac{1}{E}\begin{bmatrix} I_1 & 0 & 0 & 0 & 0 & 0 \\ 0 & I_2 & 0 & 0 & 0 & -I_3 \\ 0 & 0 & I_4 & 0 & I_5 & 0 \\ 0 & 0 & 0 & I_6 & 0 & 0 \\ 0 & 0 & I_5 & 0 & I_7 & 0 \\ 0 & -I_3 & 0 & 0 & 0 & I_8 \end{bmatrix}$$

$$C_{Az} = \frac{1}{E}\begin{bmatrix} I_1 & 0 & 0 & 0 & 0 & 0 \\ 0 & I_4 & 0 & 0 & 0 & -I_5 \\ 0 & 0 & I_2 & 0 & I_3 & 0 \\ 0 & 0 & 0 & I_6 & 0 & 0 \\ 0 & 0 & I_3 & 0 & I_8 & 0 \\ 0 & -I_5 & 0 & 0 & 0 & I_7 \end{bmatrix} \tag{15}$$

In the Type II structure, that is, the biaxial flexible hinge, the flexible hinge is a symmetrical structure, and the calculation method of the flexibility matrix is the same as that of the one-way flexible hinge, as shown in Fig. 9

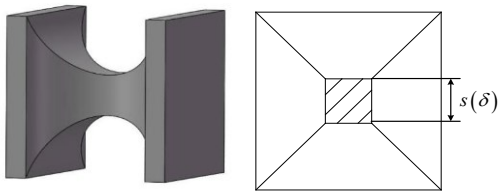

Fig. 9 Structure of type II

Where v is the Poisson's ratio of the material. The compliant matrix c of the biaxial flexible hinge is obtained [9].

$$C_B = \frac{1}{E}\begin{bmatrix} I_9 & 0 & 0 & 0 & 0 & 0 \\ 0 & I_{10} & 0 & 0 & 0 & -I_{11} \\ 0 & 0 & I_{10} & 0 & I_{11} & 0 \\ 0 & 0 & 0 & 2(\upsilon+1)I_{12} & 0 & 0 \\ 0 & 0 & I_{11} & 0 & I_{13} & 0 \\ 0 & -I_{11} & 0 & 0 & 0 & I_{13} \end{bmatrix} \tag{16}$$

In the above formula, let

$$I_9 = \int_0^{2R} \frac{1}{s(\delta)^2} d\delta \quad I_{12} = \int_0^{2R} \frac{64}{9s(\delta)^4} d\delta$$
$$I_{10} = \int_0^{2R} \frac{12\delta^2}{s(\delta)^4} d\delta \quad I_{13} = \int_0^{2R} \frac{12}{s(\delta)^4} d\delta \tag{17}$$
$$I_{11} = \int_0^{2R} \frac{12\delta}{s(\delta)^4} d\delta$$

Combined with the above calculations, the flexible hinges are combined to obtain the compliant matrices $\boldsymbol{C_A}$ and $\boldsymbol{C_B}$ of I and II types. Therefore, the equivalent compliant matrix of the flexible hinges is Eq. (18).

$$\boldsymbol{C}_{eq} = \left(\boldsymbol{C}_A^{-1} + \boldsymbol{C}_B^{-1}\right)^{-1} \tag{18}$$

The flexibility matrix relates the displacement $\boldsymbol{u'}$ at z to the load $\boldsymbol{f'}$.

$$\boldsymbol{u'} = \boldsymbol{C}_{eq}\boldsymbol{f'} \tag{19}$$

The calculated compliant matrix now requires further steps to derive the expressions of the displacement $\boldsymbol{u}$ and the load $\boldsymbol{f}$ at the center of the ends of the flexible hinge ($z=h/2$). Therefore, the relationship between the displacement and the force of the overall matrix of the flexible hinge is Eq. (20).

$$\boldsymbol{u'} = \boldsymbol{Au},\ \boldsymbol{f'} = \boldsymbol{Bf} \tag{20}$$

According to the spatial transformation of the displacement force, it can be concluded

$$\boldsymbol{A} = \begin{bmatrix} \boldsymbol{I} & \boldsymbol{k} \\ \boldsymbol{0} & \boldsymbol{I} \end{bmatrix}, \boldsymbol{B} = \begin{bmatrix} \boldsymbol{I} & \boldsymbol{0} \\ \boldsymbol{k} & \boldsymbol{I} \end{bmatrix}, \boldsymbol{k} = \begin{bmatrix} \frac{h}{2} - R & & \\ & 0 & \\ & & 0 \end{bmatrix} \tag{21}$$

Bring the Eq. (20) and Eq. (21) into Eq. (19) yields

$$\boldsymbol{u} = \left(\boldsymbol{A}^{-1}\boldsymbol{C}_{eq}\boldsymbol{B}\right)\boldsymbol{f} \tag{22}$$

Therefore, the overall complaint matrix of the flexible hinge is found as

$$\boldsymbol{C} = \boldsymbol{A}^{-1}\boldsymbol{C}_{eq}\boldsymbol{B} \tag{23}$$

In order to ensure the correctness of the analytical calculation results, this paper will use the finite element analysis software ANSYS Workbench to establish a finite element linear analysis model to compare the compliant matrix obtained above.

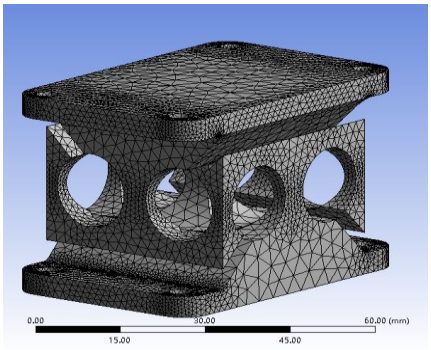

Fig. 10 Mesh of the FE model

After the end of the calculation, the elements of the compliant matrix analyzed by MATLAB are compared with the

results of the finite element software analysis by extracting the compliant matrix of the structure. In the calculation process, the material used in this paper is the high performance nylon PA12 described above, and the error of the analytical analysis model (AM) and the finite element analysis model (FEM) is obtained by an error function (Eq. (24)), as shown in TABLE II.

$$\Delta\%=100\frac{\left|C_{i,j\mathrm{AM}}-C_{i,j\mathrm{FEM}}\right|}{\left\|\boldsymbol{C}_{\boldsymbol{FEM}}\right\|_F} \tag{24}$$

TABLE III COMPARISON BETWEEN AM AND FEM COMPLIANCE FACTORS

	$C_{u_x-F_x}$ (mm/ N)	$C_{u_y-F_y}$ (mm/ N)	$C_{u_z-F_z}$ (mm/ N)	$C_{\theta_x-M_x}$ $(\mathrm{Nmm})^{-1}$	$C_{\theta_y-M_y}$ $(\mathrm{Nmm})^{-1}$	$C_{\theta_z-M_z}$ $(\mathrm{Nmm})^{-1}$	$C_{u_y-M_z}$ (N^{-1})	$C_{u_z-M_y}$ (N^{-1})
AM	1.22×10^{-4}	1.94×10^{-2}	1.94×10^{-2}	1.37×10^{-5}	3.14×10^{-5}	3.14×10^{-5}	-2.35×10^{-4}	2.35×10^{-4}
FEM	2.52×10^{-4}	2.03×10^{-2}	1.98×10^{-2}	4.75×10^{-5}	6.40×10^{-5}	4.75×10^{-5}	-9.56×10^{-4}	9.42×10^{-4}
Δ%	0.46	3.1	1.4	0.12	0.12	0.05	2.5	2.5

IV. RESULT

By comparing the results of analytical calculations and finite element calculations, it can be found that the errors in the flexibility matrix are small, indicating that the computational analysis model basically conforms to the actual deformation. Only the value of $C_{u_y-F_y}$ is more than 3%, which should be due to the fact that the model of the finite element analysis is not exactly the same as the theoretically calculated model. In the real structure, there are screw holes and support mechanisms for fixing, which is not in the analytical calculation.

(a)

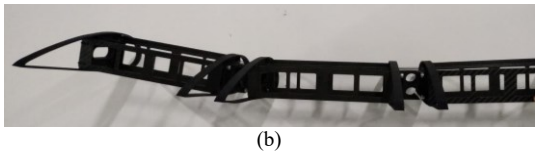

(b)

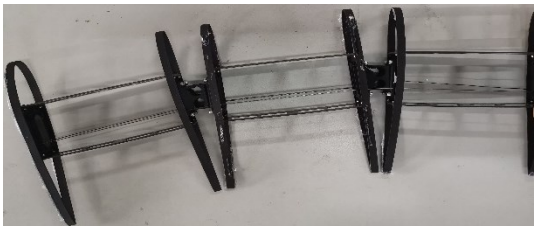

(c)

Fig. 11 (a) Wing model, (b) Deformation of spanwise, (c) Deformation of sweep

Based on the above work, the model test piece of the flexible deformed wing was fabricated and the ground test was carried out. The experimental piece has a length of 680 mm and is arranged with two 1 mm SMA wires. The SMA wire has a pre-strain of 3%. The SMA wire is heated by a constant power source. The internal heating current is 4.5A and the external heating current is 1A.

Experiments have shown that the maximum deflection displacement of spanwise on one side of the model is about 50 mm, and the corresponding deflection angle is about 7.9°. The maximum deflection displacement of sweep on one side of the model is about 45 mm, and the corresponding deflection angle is about 7.1°. The ground test also measured the time of deformation of the model, at which the deformation time was approximately 17 s.

V. CONCLUSION

A morphing wing is designed and fabricated with flexible hinge that can achieve the varying spanwise curvature and sweep angle of the wing. Compared with the traditional rigid wing structure, the design has lighter weight and no transmission clearance. And the flexible hinge of the key components of the wing is analyzed, and its analytical calculation method was obtained. The method's validation is compared by FEM method. In addition, the SMA actuator is analyzed and an improved heating method is used to improve the response speed. In addition, use a new method to heat the SMA and the varnished wire at the same time instead of heat SMA wires alone. Experiments show that the new method can heat SMA wires faster.

REFERENCES

[1] Neal, David, et al. "Design and wind-tunnel analysis of a fully adaptive aircraft configuration." *45th AIAA/ASME/ASCE/AHS/ASC Structures, Structural Dynamics & Materials Conference*. 2004.

[2] Chen, Qian, et al. "Design and analysis of a variable-sweep morphing aircraft with outboard wing section large-scale shearing." *Acta Aerodynamica Sinica* 31.1 (2013): 40-46.

[3] Gamble, Lawren L., Amin Moosavian, and Daniel J. Inman. "Effects of Speed on Coupled Sweep and Camber in Morphing Wings." *55th AIAA Aerospace Sciences Meeting*. 2017.

[4] Wiggins, Leonard, et al. "A design and analysis of a morphing hyper-elliptic cambered span (HECS) wing." *45th AIAA/ASME/ASCE/AHS/ASC Structures, Structural Dynamics & Materials Conference*. 2004.

[5] Majji, Manoranjan, and John Junkins. "Robust control of redundantly actuated dynamical systems." *AIAA Guidance, Navigation, and Control Conference and Exhibit*. 2006.

[6] Nigam N, Zhang Y, and Chen P, "Adaptive Control and Actuation System Development for Biomimetic *Morphing.*" *24th AIAA/AHS Adaptive Structures Conference. 2016.*

[7] Lobontiu, Nicolae, and Ephrahim Garcia. "Two-axis flexure hinges with axially-collocated and symmetric notches." *Computers & structures* 81.13 (2003): 1329-1341.

[8] Palmieri, G., M. C. Palpacelli, and M. Callegari. "Study of a fully compliant u-joint designed for minirobotics applications." *Journal of mechanical design* 134.11 (2012): 111003.

[9] Qiu, Lifang, Xin Yue, and Zhongtian Xie. "Design and analysis of Multicavity Flexure Hinge (MCFH) based on three-dimensional continuum topology optimization." *Mechanism and Machine Theory* 139 (2019): 21-33.